Letters

Magnetic Integration of Three-Phase Buck Converter With Three-Pointed Star Core Geometry

Zhe Zhang, *Senior Member, IEEE*, Jie Jin, *Student Member, IEEE*, Chao Liu, *Member, IEEE*, and Yu Tang, *Senior Member, IEEE*

***Abstract*—In this letter, a planar magnetically integrated inductor design method is proposed for a direct coupled three-phase interleaved Buck converter (three-phase IBC) with a three-pointed star (TPS) core geometry. Through a comparative analysis of various magnetic core structures, a TPS core featuring magnetic integration is selected, and the air gap positions are determined to effectively mitigate the eddy current loss on the PCB windings introduced by the fringing flux. Following this, the winding arrangement of the planar inductor is systematically analyzed, and an improved layout scheme is proposed, which significantly improves magnetic coupling and reduces inductor core losses. Finally, a 2 kW three-phase IBC prototype with a peak efficiency of 98.3% is built and tested. The results validate the effectiveness of the proposed design method and its theoretical analysis.**

***Index Terms*—Air gap distribution, direct coupled, magnetical integrated inductor, winding arrangement.**

I. Introduction

With the advances of wide band-gap (WBG) semiconductor devices, power converters are evolving toward higher frequency, higher efficiency, and increased power density [1], [2]. As a typical passive component which may dominate the size and weight of a power converter, planar inductors are gradually replacing traditional wound inductors, attracting growing attention [3], [4]. Numerous studies have explored different magnetic integration schemes for various converter topologies. In [5], a design approach integrating three transformers into a single core was proposed, where the leakage inductance between the primary and secondary windings served as a series inductor, achieving both structure simplification and improved power density. [6] presented a two-stage dc–dc converter in which the two-phase inductors of a Boost stage were magnetically integrated with the transformer of a downstream LLC stage. An analysis of winding arrangements was conducted to reduce losses and further optimize performance. In [7], traditional two-phase inductors were integrated into a four-leg EI-type magnetic core with optimized air gap placement, leading to reduced core loss and component size.

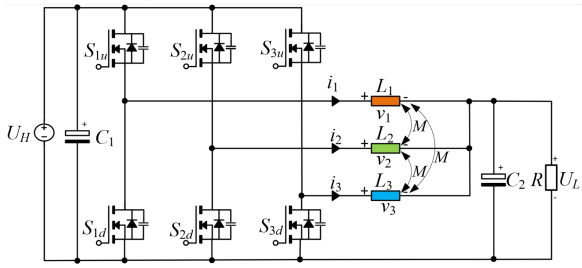

Fig. 1. Three-phase IBC topology.

In the context of multiphase converter designs, [8] introduced a cubic magnetic core integrating four inductors for a four-phase Buck converter. This structure utilized magnetic flux "peak flattening" to decrease core loss and volume while resolving current imbalance issues. In [9], I-cores are incorporated to enhance the coupling between phases and channels in interleaved three-phase ac–dc converters. As a result, the proposed modular-monolithic structure not only improves power density, but also provides additional harmonic suppression. In [10], a butterfly-style interleaved winding structure was used to develop a four-phase reverse coupled integrated inductor that effectively suppressed proximity effects. The authors in [11] proposed an integrated design of three phase integrated inductor with optimized turn numbers and air gap sizes, aiming to reduce coupling by increasing the magnetic volume. However, the influence of winding arrangement on coupling behavior and magnetic losses was not thoroughly addressed, leaving room for further optimization.

In this letter, a magnetic integration approach for the three-phase interleaved Buck converter (3-phase IBC), as shown in Fig. 1, based on a three-pointed star (TPS) core geometry is proposed and the new contributions are as follows.

1) The impact of different shaped core structures on core loss is addressed and analyzed.

Received 21 May 2025; revised 30 June 2025; accepted 9 July 2025. Date of publication 21 August 2025; date of current version 22 October 2025. Manuscript received May 21, 2025; revised July 1, 2025; accepted July 9, 2025. This work was supported by National Key Research and Development Program of China under Grant 2024YFB2504900. *(Corresponding authors: Zhe Zhang; Jie Jin; Chao Liu.)*

Zhe Zhang, Jie Jin, and Yu Tang are with the State Key Laboratory of Intelligent Power Distribution Equipment and System, Hebei University of Technology, Tianjin 300401, China (e-mail: 2021060@hebut.edu.cn; 202411401016@stu.hebut.edu.cn; 2018040@hebut.edu.cn).

Chao Liu is with the Department of Wind and Energy Systems, Technical University of Denmark, 2800 Kongens, Denmark (e-mail: chali@dtu.dk).

Color versions of one or more figures in this article are available at https://doi.org/10.1109/TPEL.2025.3601370.

Digital Object Identifier 10.1109/TPEL.2025.3601370

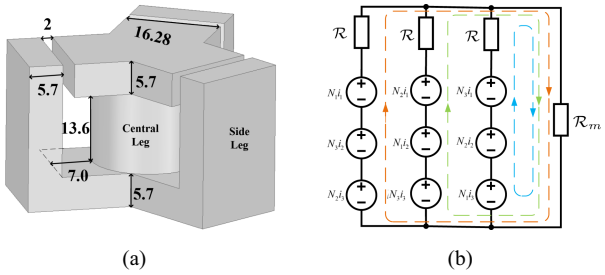

Fig. 2. Magnetic core structure and reluctance model. (a) Magnetic core diagram, unit (mm). (b) Reluctance equivalent circuit.

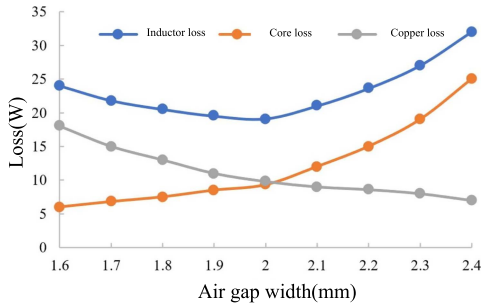

Fig. 3. Relationship between inductor loss and air gap length.

2) The position of the air gap is systematically designed based on performance evaluation.
3) A comparative analysis of various winding arrangements is conducted, leading to the identification of the improved winding configuration.

II. Magnetic Integration Theory Analysis

For the integration of the three-phase IBC direct coupled inductors, this letter proposes a magnetically integrated structure in which three inductors are symmetrically arranged at 120° intervals, and each winding is placed clockwise with N_1 turns on one of the side limbs of the core, while the other two windings, with N_2 and N_3 turns respectively, are distributed on the rest two magnetic legs.

The detailed magnetic core structure and its corresponding equivalent magnetic reluctance model are illustrated in Fig. 2. The reluctance of the air gap is significantly higher than that of the magnetic core, causing the main magnetic flux to complete its path predominantly through the central circular leg. Since the currents in the three-phase windings are equal in magnitude and phase-shifted by 120°, the net magnetic flux variation–particularly in the central leg of the core–is significantly reduced, resulting in improved magnetic flux cancellation and therefore lower core loss. Based on the reluctance model, the inductance characteristics of the three-phase coupled inductor can be represented, as shown as follows:

$$L = \begin{bmatrix} L_{11} & M_{12} & M_{13} \\ M_{12} & L_{22} & M_{23} \\ M_{31} & M_{32} & L_{33} \end{bmatrix} \tag{1}$$

where L_{ii} denotes the self-inductance of phase i, and M_{ij} denotes the mutual inductance between phases i and j. The corresponding formula is expressed as follows:

$$L_{ii} = \sum_{j=1}^{3} \frac{N_j^2}{\mathcal{R}+3\mathcal{R}_m} \cdot \frac{\mathcal{R}+2\mathcal{R}_m}{\mathcal{R}} \approx \sum_{j=1}^{3} \frac{N_j^2}{\mathcal{R}} \tag{2}$$

$$M_{ij} = \sum_{0<m<n}^{3} \frac{N_m N_n (\mathcal{R}+2\mathcal{R}_m)}{(\mathcal{R}+3\mathcal{R}_m)\mathcal{R}} \approx \sum_{0<m<n}^{3} \frac{N_m N_n}{\mathcal{R}} \tag{3}$$

where $\mathcal{R}$ and $\mathcal{R}_m$ denote the magnetic reluctance of each phase core and the air gap, respectively, with $\mathcal{R}_m \gg \mathcal{R}$.

Then, the coupling coefficient k can be calculated as follows:

$$k = \frac{N_1N_2 + N_2N_3 + N_1N_3}{N_1^2 + N_2^2 + N_3^2}. \tag{4}$$

In the three-phase IBC, the introduction of direct coupling reduces the sum of the three-phase inductor currents by a factor of $(1+2k)$ compared to the uncoupled case, as shown in (5). A higher coupling coefficient k thus leads to lower total current ripple, improving current control accuracy and filtering performance

$$\frac{\Delta I_{cpl}}{\Delta I_{uncpl}} = \frac{1}{(1+2k)} \tag{5}$$

where ΔI_{cpl} and ΔI_{uncpl} represent the sum of the three-phase inductor currents under coupled and uncoupled conditions, respectively.

According to (6), a larger k demands a higher switching frequency (f_{sw}) to keep single phase inductor current ripple Δi constant. To ensure the ripple remains within a controllable range, a switching frequency of 250 kHz is selected for inductor design, with a 50 kHz margin. The required self-inductance can be calculated $L_{ii} = 17.3\,\mu$H. For $f_{\text{sw}} = 300$ kHz, the coupling coefficient should be limited to $k \leq 0.21$ to ensure stability and acceptable ripple performance

$$\Delta i = \frac{(U_H - U_L)D}{\frac{(1-k)(1+2k)}{1+\left(1+\frac{2D}{1-D}\right)k} L_{ii} f_{sw}}. \tag{6}$$

Based on the magnetic core structure shown in Fig. 2(a), an iterative magnetic design is performed to achieve $L_{ii} = 17.3\,\mu$H by adjusting the winding turns and air gap length. The relationship between copper/core loss and air gap is illustrated in Fig. 3, indicating that an air gap of 2 mm yields the optimal trade-off. At this point, the required number of primary turns is $N_1 = 10$, and according to (4), the resulting winding turn ratio is 10:1:1.

III. Magnetic Integration of Three-Phase Direct Coupled Inductors

A. Magnetic Core Design

Compared to discrete magnetic cores, integrated magnetic cores exhibit certain differences in the magnetic flux return path. Moreover, the geometric design of the core's top and bottom regions significantly influences the distribution and direction

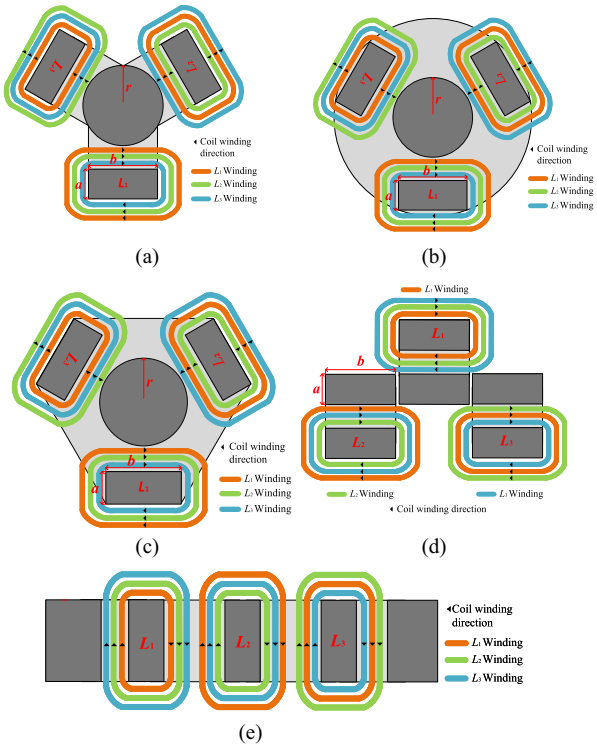

Fig. 4. Schematic of magnetic core structure and winding configuration. (a) TPS core. (b) Round core. (c) Hexagonal core. (d) Discrete core. (e) Matrix core.

TABLE I
PARAMETERS OF DIFFERENT STRUCTURES

Core Geometry	Volume mm^3	Core Loss W	Copper Loss W
TPS Core	18000	12.17	11.43
Round Core	26775	11.13	12.07
Hexagonal Core	22413	11.78	11.55
Matrix Core	21862	7.30	20.21
Discrete Core	17816	15.73	18.16

of magnetic flux. Therefore, this letter analyzes the impact of the magnetic core structure on core loss, considering various configurations, including TPS, round, hexagonal, matrix, and discrete core as shown in Fig. 4.

In this letter, the simulation is carried out using the Maxwell finite element (FEM) software. And the simulation parameters are set as follows: a 300 kHz current with a peak value of 20 A is used as the excitation source. Magnetic integration leads to a 27.4% reduction in inductor core loss, as summarized in Table I. As shown in Fig. 5, the magnetic flux is most concentrated at the junction between the winding legs and the base in all four designs. In the comparison among Fig. 5(a)–(c), although the TPS core exhibits a slightly higher flux density in the base region, the difference in core loss among the three remains within 8.5%, and the TPS core requires the smallest volume.

The matrix core achieves a 40.90% lower core loss than the TPS core, owing to its extended magnetic path and improved flux cancellation. However, its copper loss is 76.91% higher than that of the TPS design, due to the distributed air gaps that generate

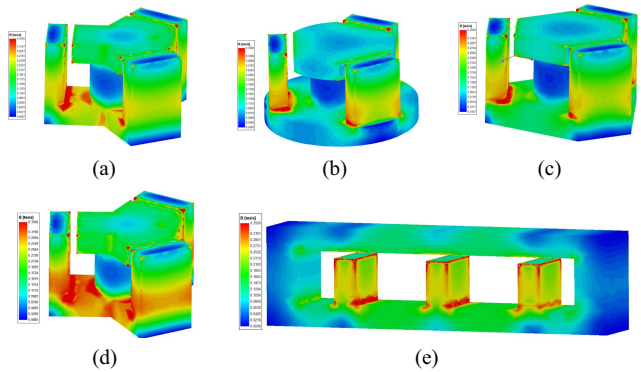

Fig. 5. Comparison of magnetic flux distribution: (a) TPS core. (b) Round core. (c) Hexagonal core. (d) TPS core with no auxiliary windings. (e) Matrix core.

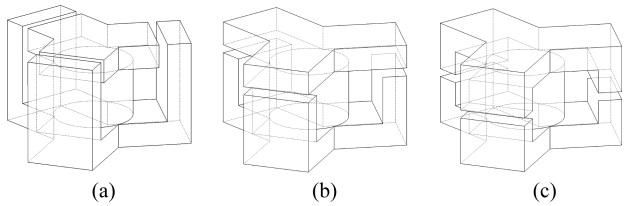

Fig. 6. Air gap position of inductor. (a) Top. (b) Upper side. (c) Middle.

significant stray flux. This leakage flux penetrates adjacent phase windings, increasing their ac resistance and resulting in higher overall copper loss. Therefore the TPS core is deemed the optimal choice.

Beyond core shape optimization, the introduction of auxiliary windings presents a trade-off between copper and core losses. Specifically, the copper loss increases from 9.41 to 11.43 W due to the extended conductor length. The magnetic flux distributions of the core, with and without auxiliary windings, are illustrated in Fig. 5(a) and (d). The auxiliary windings partially cancel the main flux generated by the self-windings along the central leg, effectively reducing the core loss from 17.67 to 12.17 W. Despite the increase in copper loss, the total loss is reduced by 7.5%, demonstrating the effectiveness of magnetic integration. Moreover, the auxiliary windings help alleviate magnetic saturation and contribute to improved overall system performance.

B. Analysis of Air Gap Position

To minimize the impact of edge effects caused by the air gap on the magnetic field distribution and overall inductor performance, thereby reducing copper loss. This letter proposes three different air gap positions, as shown in Fig. 6. FEM simulation of the model were conducted using Maxwell. The simulation results are shown in Fig. 7, which illustrates the current density distribution of the winding under different air gap positions.

Case I: To reduce the impact of edge effects, the windings are placed below the core window. The current density distribution for this configuration is shown in Fig. 7(a). It can be observed that the winding current density is relatively uniform, with minimal

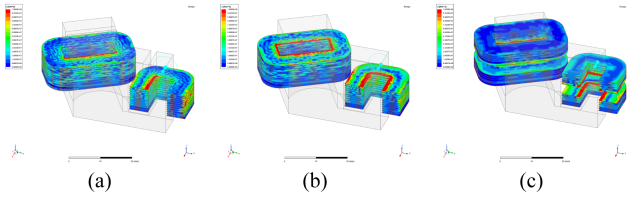

Fig. 7. Simulation of the effect of air gap position on winding current density. (a) Top. (b) Upper side. (c) Middle.

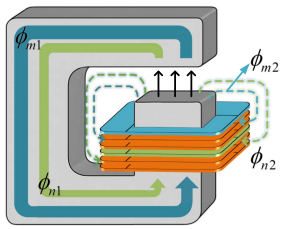

Fig. 8. Main and leakage fluxes of different windings.

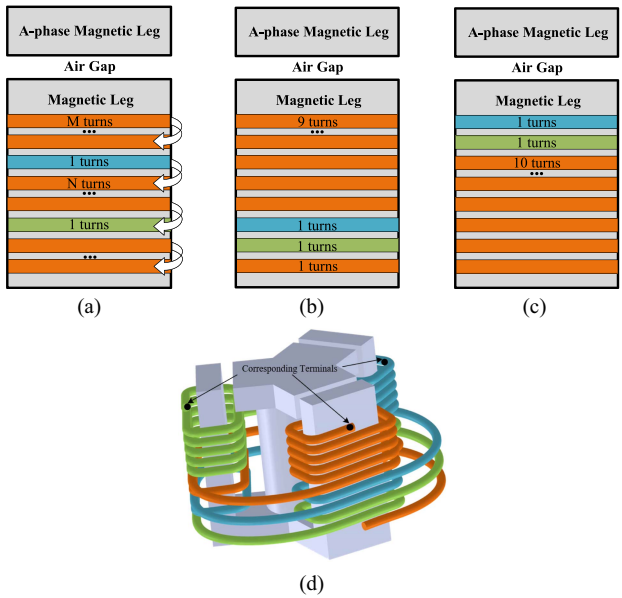

Fig. 9. Comparison of winding arrangements. (a) Benchmark configuration. (b) Proposed configuration. (c) Worst-case configuration. (d) Physical configuration of the windings.

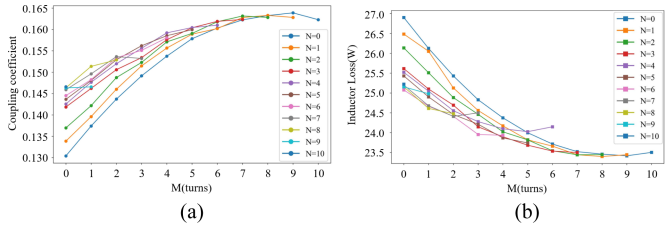

Fig. 10. Comparison of the air gap position. (a) Coupling coefficient. (b) Inductor loss.

edge effect near the air gap. The current distribution is balanced, resulting in reduced copper loss.

Case II: The windings are still placed below the core window. Fig. 7(b) displays the current density distribution in this configuration. Compared to the Case I the edge effects around the air gap become more pronounced, leading to increased local current density nonuniformity, particularly in the region below the air gap, where the current density is higher. Moreover, the area affected by the air gap expands, and although the edge effect is smaller compared to the Case III, it still causes significant losses.

Case III: To minimize the impact of the air gap on the winding, the windings are distributed on both the upper and lower sides of the core window. The current density distribution is shown in Fig. 7(c). In this case, the edge effects near the air gap affect both the upper and lower windings, leading to a significantly uneven current density distribution. The areas close to the air gap exhibit higher current densities, and the region influenced by the air gap, as well as the number of winding turns affected, are the largest. This results in increased ac resistance, significantly raising the copper loss of the planar magnetic integrated inductor.

C. Winding Arrangement Analysis

As magnetic flux in PCB inductors concentrates near the air gaps, leakage flux is assumed to occur only at these locations. As illustrated in Fig. 8, the leakage flux caused by the air gap penetrates multiple winding layers. Specifically, the leakage flux Φ_{m2} generated by the Mth layer winding (in blue), from top to bottom, mainly closes through its adjacent winding paths, while the more distant N-th layer winding (in green) is almost unaffected. In contrast, the flux generated by the Nth layer almost entirely closes through the Mth layer path. Therefore, the magnetic coupling strength between the Mth and Nth layers exhibits a clear asymmetry. This characteristic indicates that the arrangement order of the windings has a significant impact on the interlayer coupling coefficient and the inductor loss.

Fig. 9(a) illustrates several constructed "sandwich"-type winding models. The winding direction is indicated by the arrows, and the same winding direction is adopted in the other configurations, though not explicitly shown. By adjusting the number of layers M where phase A is placed above phase B, and the number of layers N where the phase A winding is inserted between phases B and C, several distinct interlayer layout schemes were formed. Based on finite element simulations, the coupling coefficients and inductor losses under different winding arrangements were calculated and compared.

The specific simulation results are presented in Fig. 10. The winding configuration with $M = 9$ and $N = 0$, shown in Fig. 9(b), yields the maximum achievable coupling coefficient of 0.162 among phase windings. As discussed in Section II, optimal performance is achieved when k approaches 0.21. Therefore, this configuration is selected as the optimal arrangement to approach the desired coupling level. In contrast, the worst performance is observed when M=0 and N=0, as shown in Fig. 9(c). These results suggest that, in the design of magnetically coupled inductors, windings with fewer turns should be placed on the

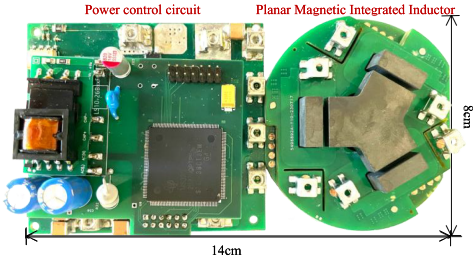

Fig. 11. Photograph of the converter.

TABLE II
KEY PARAMETERS OF THE PROTOTYPE

Parameters	Value	Parameters	Values
Transistor	Inn650d080bs	P_o	2 kW
V_{in}	133-400 V	V_o	100 V
Load	5 Ω	k	0.16
C_{in}	17 μF	C_{out}	12.1 μF
f_{sw}	100-290 kHz	L	16.66 μH

bottom layers, and an interleaved (cross-layer) arrangement should be employed to achieve optimal electromagnetic performance. Accordingly, Fig. 9(d) illustrates the detailed winding configuration corresponding to Fig. 9(b), with corresponding terminals marked to ensure direct coupling among the three phases.

IV. RESULTS AND ANALYSIS

To verify the rationality of the proposed design, a three-phase IBC prototype was developed, as shown in Fig. 11. The dimensions of the converter are 14 cm × 8 cm × 2.5 cm. The detailed specifications of the converter are listed in Table II.

Fig. 12 shows the experimental waveforms of the inductor current under full load at U_H=400 V and 133 V, respectively. In the waveforms, U_{S_1u} represents the voltage between the drain and source of the switch S_{1u}. It can be observed that the valley current of the inductor reaches −2 A and soft switching is successfully achieved in all cases.

Fig. 13 shows the thermal image of the TPS inductor operating at full load with enhanced forced-air cooling. The maximum temperature of the PCB windings reached 51.5 °C, while the core temperature remained at 36.5 °C. The result confirms that the temperature rise is well within an acceptable range.

Fig. 14(a) presents the efficiency curves of the converter under input voltages of 133 V, 200 V, and 400 V. At an input voltage of 133 V, the converter reaches its peak efficiency of 98.3% . The corresponding loss breakdown at this operating point is depicted in Fig. 14(b). As illustrated, the inductor loss–encompassing both copper and core losses–together with the MOSFET switching device loss constitute approximately 80% of the total power loss. This highlights the importance of carefully addressing these two loss components in the design of a three-phase IBC to improve overall system efficiency, thermal management, and power density.

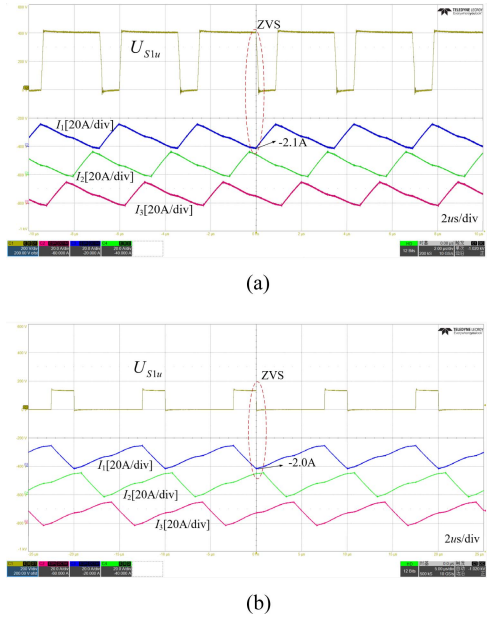

Fig. 12. Three-phase inductor current waveforms under different duty cycles. (a) D = 0.33. (b) D = 0.75.

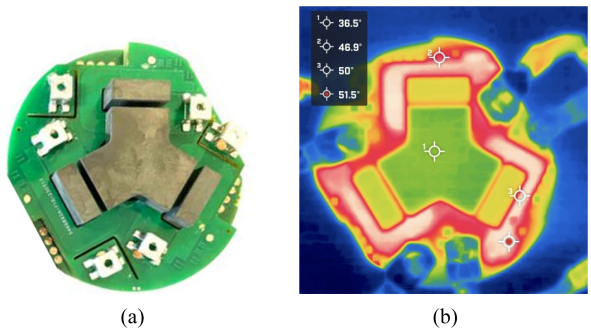

Fig. 13. Physical and thermal photograph of the TPS inductor. (a) Physical image. (b) Thermal image.

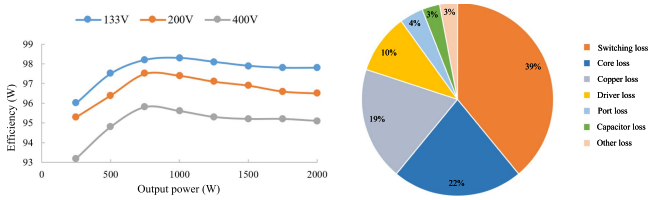

Fig. 14. System efficiency distribution. (a) Efficiency curve versus output power. (b) Loss distribution diagram.

V. CONCLUSION

With the unique TPS core geometry, a high efficient planar integrated magnetics design approach for three-phase IBC. A planar magnetic integrated inductor design method is proposed for direct coupled inductors, and a TPS core structure is developed accordingly. By optimizing the air gap position, the edge effect around the gap is effectively suppressed, significantly

reducing its impact on the current density distribution in PCB windings and thereby lowering copper losses. An improved winding strategy is also presented, which enhances the coupling coefficient of the integrated inductor without changing the winding configuration. To validate the theoretical analysis and design methodology, a 2 kW prototype of a three-phase IBC converter was developed. Experimental results show that the converter achieves a peak efficiency of 98.3%, fully demonstrating the correctness and superiority of the proposed planar magnetic integration design method.

REFERENCES

[1] J. Ning, Y. Sun, J. Lin, G. Xu, and M. Su, "ExtendedFilippov'smethodfor stability analysis of digitally controlled DC-DC converters," *IEEE Trans. Ind. Electron.*, vol. 71, no. 8, pp. 9426–9435, Aug. 2023.

[2] H. Wang et al., "Stability analysis of series-capacitor buck converters with different phase shift strategies via Filippov's method," *IEEE Trans. Power Electron.*, vol. 40, no. 9, pp. 12964–12976, Sep. 2025.

[3] Y. Liu, H. Wu, Z. Ge, and G. Ji, "Magnetic integration for multiple resonant converters," *IEEE Trans. Ind. Electron.*, vol. 70, no. 8, pp. 7604–7614, Aug. 2023.

[4] Y. Cai, M. H. Ahmed, Q. Li, and F. C. Lee, "Optimal design of megahertz *LLC* converter for 48-V bus converter application," *IEEE J. Emerg. Sel. Topics Power Electron.*, vol. 8, no. 1, pp. 495–505, Mar. 2020.

[5] Z. Zhang, J. Huang, and Y. Xiao, "GaN-based 1-MHz partial parallel dual active bridge converter with integrated magnetics," *IEEE Trans. Ind. Electron.*, vol. 68, no. 8, pp. 6729–6738, Aug. 2021.

[6] P. Wang, A. Arruti, J. Huang, T. G. Zsurzsan, M. A. E. Andersen, and Z. Ouyang, "Integrated magnetic design for high power density converter," in *Proc. IEEE Appl. Power Electron. Conf. Expo.*, Long Beach, CA, USA, 2024, pp. 3235–3241.

[7] Y. Liu et al., "Optimized air-gap configuration for an integrated coupled inductor with lower height and reduced core/winding losses," *IEEE Trans. Ind. Appl.*, vol. 60, no. 2, pp. 2980–2990, Mar./Apr. 2024.

[8] A. D. Nguyen, C.-W. Chen, J.-S. Lai, and Y.-C. Liu, "Matrix inductor with DC-bias effect reduction capability for GaN-based DC-DC boost converter," *IEEE Trans. Circuits Syst. II, Exp. Briefs*, vol. 67, no. 11, pp. 2597–2601, Nov. 2020.

[9] R. Phukan, D. Nam, D. Dong, R. Burgos, G. Mondal, and S. Nielebock, "Highly integrated monolithic filter building block for SiC based three-phase interleaved converters," in *Proc. IEEE Appl. Power Electron. Conf. Expo.*, Phoenix, AZ, USA, 2021, pp. 2876–2882.

[10] M. Li, Y. Liu, Z. Ouyang, and M. A. E. Andersen, "Butterfly interleaving winding arrangements for multiphase coupled inductors," *IEEE Trans. Power Electron.*, vol. 38, no. 3, pp. 3315–3327, Mar. 2023.

[11] Y.-C. Liu, C. Chen, Y.-C. Chung, M.-C. Tsai, and K. A. Katherine, "Integrated magnetics design for an interleaved three-phase buck converter," in *Proc. IEEE Energy Convers. Congr. Expo.*, Detroit, MI, USA, 2020, pp. 4533–4538.